PHYSICAL REVIEW MATERIALS **6**, 094010 (2022)

Impurity-induced excitations in a topological two-dimensional ferromagnet/superconductor van der Waals moiré heterostructure

Maryam Khosravian and Jose L. Lado
Department of Applied Physics, Aalto University, 02150 Espoo, Finland

(Received 12 April 2022; revised 17 August 2022; accepted 6 September 2022; published 23 September 2022)

The emergence of a topological superconducting state in van der Waals heterostructures provides a new platform for exploring novel strategies to control topological superconductors. In particular, impurities in van der Waals heterostructures, generically featuring a moiré pattern, can potentially lead to the unique interplay between atomic and moiré length scales, a feature absent in generic topological superconductors. Here we address the impact of nonmagnetic impurities on a topological moiré superconductor, both in the weak and strong regime, considering both periodic arrays and single impurities in otherwise pristine infinite moiré systems. We demonstrate a fine interplay between impurity-induced modes and the moiré length, leading to radically different spectral and topological properties depending on the relative impurity location and moiré lengths. Our results highlight the key role of impurities in van der Waals heterostructures featuring moiré patterns, revealing the key interplay between length and energy scales in artificial moiré systems.

DOI: 10.1103/PhysRevMaterials.6.094010

I. INTRODUCTION

The design of artificial topological superconductors is one of the most active areas in designer quantum materials [1–15], fueled by their fundamental interest and their potential for future topological computing architectures [16–19]. Engineering topological superconductivity requires three different ingredients, magnetism, spin-orbit coupling, and superconductivity, features that have been harvested in a variety of platforms, including semiconducting nanowires [20–22], atomic chains [5,23], topological insulators [24,25], and van der Waals materials [26–28]. In particular, besides all the rich physics of topological superconductors, van der Waals topological superconductors such as $\mathrm{CrBr_3/NbSe_2}$ heterostructures [26–28] display a unique feature stemming from their van der Waals nature [29,30], the emergence of a moiré pattern.

Artificial van der Waals topological superconductors, and moiré heterostructures in general, display two length scales, the original lattice constant and the emergent moiré length [31–35]. The existence of a moiré pattern leads to a superconducting state with an associated moiré electronic structure, and more importantly, a spatially modulated structure directly inherited from the moiré pattern [36,37]. In particular, atomic defects in two-dimensional materials including substitutional elements and vacancies have a relevant length scale stemming from the microscopic lattice constant [38–42], and therefore can give rise to a rich interplay with the moiré length. While impurities in uniform topological superconductors have been widely studied [43–49], the interplay between local impurities in moiré systems has remained relatively unexplored [50–53].

In this paper, we address the impact of nonmagnetic impurities on artificial moiré topological superconductors. We show that interplay between the moiré pattern and local impurities gives rise to radically different impacts of the defects depending on the specific location. Our paper is organized as follows. First, in Sec. II we introduce the model for a moiré topological superconductor. In Sec. III we address the impact of strong impurities in the topological state. In Sec. IV we address the impact of weak impurities in the moiré superconductor. In Sec. V we study the interplay between the amplitude of the moiré pattern and the location of the impurity. In Sec. VI we address the emergence of in-gap modes for single impurities in otherwise pristine systems. In Sec. VII we examine the emergence of topological moiré edge modes in the defective and pristine topological moiré superconductor. Finally, in Sec. VIII we summarize our conclusions.

II. MODEL

Here we will consider a generic topological superconductor realized in a van der Waals heterostructure, as realized in a $\mathrm{CrBr_3/NbSe_2}$ heterostructure [26]. In this material, the relative lattice mismatch and rotation between the $\mathrm{CrBr_3}$ ferromagnet and the $\mathrm{NbSe_2}$ superconductor leads to the emergence of a moiré pattern, as shown in Fig. 1(a). In particular, the moiré pattern is expected to directly impact the underlying Hamiltonian of the system due to the local structural modulation [54–58]. Such a modulation directly imprints Yu-Shiba-Rusinov states following the moiré pattern [28]. Due to the structural modulation, including the local hoppings [59], induced spin-orbit coupling [54], chemical potential [60], exchange field [61], and superconducting proximity [62] will be modulated. For the sake of concreteness, here we will focus on the two parameters whose modulation is expected to be most sizable, the local superconducting order and the proximity-induced exchange field. It is worth noting that, beyond the currently realized $\mathrm{CrBr_3/NbSe_2}$ heterostructure displaying topological superconductivity [26–28], a variety of

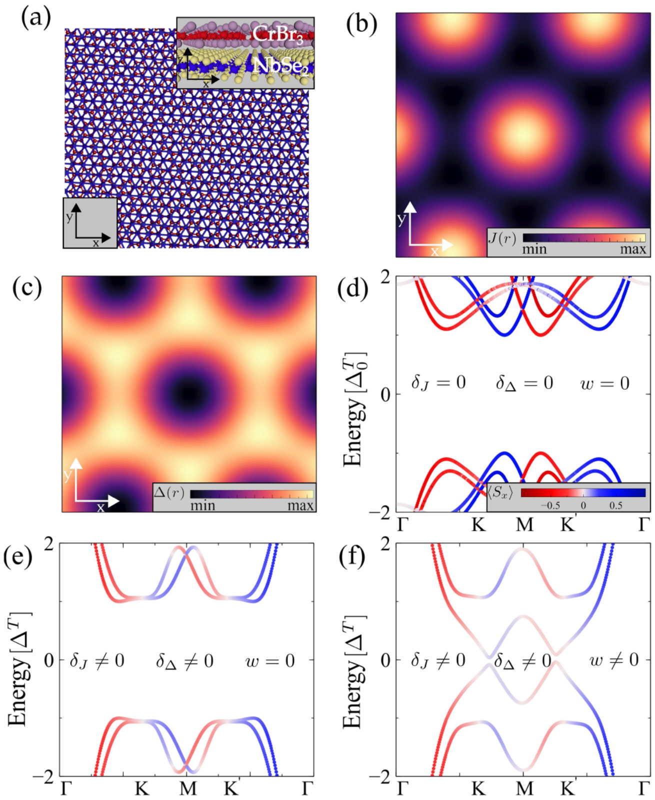

FIG. 1. (a) Schematic view of an artificial $CrBr_3/NbSe_2$ moiré topological superconductor. Panels (b) and (c) show the real-space modulation of exchange coupling $J(\mathbf{r})$ (b) and superconductivity $\Delta(\mathbf{r})$ (c) in the moiré unit cell. Panels (d), (e), and (f): Electronic band structure of a (d) uniform, (e) moiré, and (f) moiré with an impurity topological superconductor. We used $J_0 = 2\Delta_0$, $\lambda = 2\Delta_0$, $\mu = 3t$, $\delta_J = 2J_0$, $\delta_\Delta = 1.4\Delta_0$.

other artificial van der Waals systems can potentially lead to topological superconductivity. As two-dimensional ferromagnets, materials such as $CrBr_3$ [63], CrI_3 [64], and $CrBr_{3-x}I_x$ [65] provide potential out-of-plane ferromagnetic monolayers, whereas $NbSe_2$ [66], NbS_2 [67], TaS_2 [68], and $TaSe_2$ [69] and their alloys [70] would provide van der Waals superconductors. For all the combinations between ferromagnets and superconductors above, the resulting heterostructure will show a moiré pattern between a honeycomb ferromagnet and a triangular superconductor, displaying an approximate C_3 rotational symmetry.

With the previous platforms in mind, we now turn to address a minimal effective model for the previous heterostructures. While the specific parameters of the model for each material combination should be estimated using first-principles calculations [54–58], here we will focus on addressing the universal features that arise due the interplay of the moiré superconductor and the local impurities [50–53]. The structure moiré pattern directly gives rise to a modulation in the induced exchange coupling and an s-wave superconductivity, whose spatial profiles are shown in Figs. 1(b) and 1(c). The electronic structure of the heterostructure is modeled with an atomistic Wannier orbital per Nb site forming a triangular lattice, where the moiré pattern is incorporated in the modulation of the Hamiltonian parameters. The full Hamiltonian takes the form

$$\mathcal{H}_0 = \mathcal{H}_{\text{kin}} + \mathcal{H}_J + \mathcal{H}_R + \mathcal{H}_{\text{SC}} \tag{1}$$

with

$$\mathcal{H}_{\text{kin}} = t \sum_{\langle ij \rangle, s} c^\dagger_{i,s} c_{j,s} + \sum_i \mu(\mathbf{r}) c^\dagger_{i,s} c_{i,s}, \tag{2}$$

where $c^\dagger_{n,s}$ ($c_{n,s}$) denotes the creation (annihilation) fermionic operator with spin s in site n, t is the hopping parameter, $\langle i, j \rangle$ runs over nearest neighbors, and μ is the chemical potential. The term

$$\mathcal{H}_J = \sum_{i,s,s'} J(\mathbf{r}) \sigma_z^{s,s'} c^\dagger_{i,s} c_{i,s'} \tag{3}$$

is the exchange coupling induced by the underlying ferromagnet, obtained by integrating out the degrees of freedom of the magnetic monolayer. The term

$$\mathcal{H}_R = i\lambda \sum_{\langle ij \rangle, ss'} \mathbf{d}_{ij} \cdot \sigma^{s,s'} c^\dagger_{i,s} c_{j,s'}, \tag{4}$$

is the Rashba spin-orbit coupling arising due to the broken mirror symmetry at the $NbSe_2/CrBr_3$ interface, σ are the spin Pauli matrices, λ controls the spin-orbit coupling constant and $\mathbf{d}_{ij} = \mathbf{r}_i - \mathbf{r}_j$. The term

$$\mathcal{H}_{\text{SC}} = \sum_i \Delta(\mathbf{r}) c^\dagger_{i,\uparrow} c^\dagger_{i,\downarrow} + \text{H.c.} \tag{5}$$

is the s-wave superconducting order. $J(\mathbf{r})$ and $\Delta(\mathbf{r})$ parametrize the exchange coupling and induced s-wave superconductivity.

Local nonmagnetic impurities are included adding a potential scattering term of the form

$$\mathcal{H}_{\text{imp}} = w \sum_s c^\dagger_{n,s} c_{n,s}, \tag{6}$$

where $\mathcal{H}_{\text{imp}}$ defines the impurity Hamiltonian at site n with an on-site potential w. The full Hamiltonian of the defective system takes the form

$$\mathcal{H} = \mathcal{H}_0 + \mathcal{H}_{\text{imp}}. \tag{7}$$

As noted above, the moiré profile in our effective model arises from the combination of modulated exchange coupling and s-wave superconductivity [71]. The interplay between the exchange field and the superconducting order, as two competing orders, results in an opposite modulated superconductivity and therefore exhibits a modulated moiré pattern in the whole platform. We account for this by defining a potential in real space with the functional form of

$$f(\mathbf{r}) = c_0 + c_1 \sum_{n=1}^{3} \cos(R^n \mathbf{q} \cdot \mathbf{r}), \tag{8}$$

where $\mathbf{q}$ is the moiré superlattice wave vector, R_n is the rotation matrix which conserves C_3 symmetry, and c_0, c_1 are chosen so that $f(\mathbf{r}) \in (0, 1)$. The spatial profiles $J(\mathbf{r})$ and $\Delta(\mathbf{r})$ are written in terms of the previous spatial dependence as

$$\begin{aligned} J(\mathbf{r}) &= J_0 + \chi \delta_J f(\mathbf{r}), \\ \Delta(\mathbf{r}) &= \Delta_0 + \chi \delta_\Delta [1 - f(\mathbf{r})]. \end{aligned} \tag{9}$$

J_0 and Δ_0 control the average magnitude of the modulated exchange and superconducting profiles, whereas δ_J and δ_Δ control the amplitude of the moiré modulation, respectively. We introduce $\chi \in (0, 1)$ as a parameter which allows us to adiabatically switch between a uniform or moiré system, and here it is taken to be 1. As noted above, the relative signs of $f(\mathbf{r})$ in $J(\mathbf{r})$ and $\Delta(\mathbf{r})$ are taken so that when the exchange is maximum, the local superconducting order is minimum. We now elaborate on the mechanism that yields those two parameters as the dominating modulations. The stacking heavily influences the value of the exchange, and ultimately it can also impact its sign [72,73]. This strong modulation of the exchange directly affects the local superconducting order, as a finite exchange field locally quenches the s-wave pairing. Therefore the superconducting and exchange modulations are anticorrelated. This is the behavior directly expected from the pair-breaking effect of the exchange field in an s-wave superconductor [74,75], and arises naturally from a self-consistent treatment of the superconducting state in the presence of the moiré modulated exchange. Experimentally, the impact of moiré modulations in $\mathrm{NbSe_2/CrBr_3}$ has been directly observed by imaging the spatial dependence of the Yu-Shiba-Rusinov bands at energies inside the gap, directly reflecting the modulation of the exchange coupling [28]. We note that, for the superconductor taken as $\mathrm{NbSe_2}$, the closest saddle point to the Fermi energy that will have the strongest moiré effect is located at the M point [76]. Finally, of course the moiré can also influence the other parameters, but their effect is expected to be be substantially smaller in comparison with the exchange field.

We now briefly elaborate in the procedure to solve the previous Hamiltonian. We take as starting point the effective Hamiltonian for a periodic moiré supercell, that takes the form

$$\mathcal{H} = \sum \Gamma^{\alpha,\beta}_{i,j,s,s'} c^\dagger_{i,\alpha,s} c_{j,\beta,s'} + \sum (\Delta_\alpha c^\dagger_{i,\alpha,\uparrow} c^\dagger_{i,\alpha,\downarrow} + \text{H.c.}), \tag{10}$$

where $c^\dagger_{i,\alpha,s}$ denotes the creation operator at unit cell i, site α, and spin s, and $\Gamma^{\alpha,\beta}_{i,j,s,s'}$ contains the hopping, spin-orbit coupling, and exchange proximity effects. The previous Hamiltonian, periodic in the supercell, can be diagonalized by defining the Bloch operators

$$c_{j,\alpha,s} = \sum_{\mathbf{k}} e^{i\mathbf{k}\cdot\mathbf{R_j}} c_{\mathbf{k},\alpha,s}, \tag{11}$$

leading to the Hamiltonian in momentum space

$$\mathcal{H} = \sum \Gamma^{\alpha,\beta}_{s,s'}(\mathbf{k}) c^\dagger_{\mathbf{k},\alpha,s} c_{\mathbf{k},\beta,s'} + \sum (\Delta_\alpha c^\dagger_{\mathbf{k},\alpha,\uparrow} c^\dagger_{-\mathbf{k},\alpha,\downarrow} + \text{H.c.}), \tag{12}$$

where $\Gamma^{\alpha,\beta}_{s,s'}(\mathbf{k})$ is the Fourier transform in the unit cell indexes i, j of the matrices $\Gamma^{\alpha,\beta}_{i,j,s,s'}$. To diagonalize the previous Hamiltonian, we define new fermionic operators $c^\dagger_{\mathbf{k},s} \equiv (c^\dagger_{\mathbf{k},1,s}, \dots, c^\dagger_{\mathbf{k},n,s})$ and $\Psi^\dagger_{\mathbf{k}} = (c^\dagger_{\mathbf{k},\uparrow}, c^\dagger_{\mathbf{k},\downarrow}, c_{-\mathbf{k},\downarrow}, c_{-\mathbf{k},\uparrow})$. The Hamiltonian in this basis can be written as

$$\mathcal{H} = \frac{1}{2} \sum \Psi^\dagger_{\mathbf{k}} H_{BdG} \Psi_{\mathbf{k}}, \tag{13}$$

where the Bogoliubov–de Gennes (BdG) Hamiltonian H_{BdG} is diagonalized in terms of the new operators, leading to a diagonal form

$$\mathcal{H} = \frac{1}{2} \sum \epsilon_{\mathbf{k},\alpha} \Psi^\dagger_{\mathbf{k},\alpha} \Psi_{\mathbf{k},\alpha}, \tag{14}$$

where $\epsilon_{\mathbf{k},\alpha}$ are the BdG eigenvalues and $\Psi^\dagger_{\mathbf{k},\alpha}$ the BdG eigenstates.

In practice, the calculation of the electronic structure for a moiré supercell requires diagonalizing a $4n \times 4n$ matrix, with n the number of sites per supercell. To compute the electronic structure in a ribbon geometry, an analogous procedure to the one outlined above is carried out for the supercell of the nanoribbon, that contains several moiré unit cells. Finally, to compute surface spectral functions, the embedding formalism described later in the paper is directly applied to the matrices defined by the BdG Hamiltonian.

It is instructive to first look at the electronic structure and topological character of the uniform system of Eq. (1) when the moiré potential is switched off. For the Hamiltonian parameters we choose the following setup: $J_0 = 2\Delta_0$, $\lambda = 2\Delta_0$, and the chemical potential set to $\mu = 3t$. In the uniform limit, for a supercell of size 9×9 as shown in Fig. 1(d), the system shows a finite gap of topological character, where the energy is measured in terms of the topological gap of the uniform system Δ_0^T. This topological superconducting gap is obtained by taking appropriate ratios of the exchange field, Rashba spin-orbit coupling, superconducting order, and chemical potential, and features a topological gap with Chern number $C = 2$ [26].

Keeping the same average values of the exchange, superconductivity, Rashba spin-orbit coupling, and chemical potential, we now move on to the moiré system, switching on the exchange and superconducting modulation δ_J and δ_Δ, which are set to $\delta_J = 2J_0$, $\delta_\Delta = 1.4\Delta_0$. The electronic structure of the modulated system is shown in Fig. 1(e), and features a topological gap with Chern number $C = 2$, where the energy is measured in terms of the topological gap of the moiré system Δ^T. We note that there is not a simple analytic relation between both gaps, and in our calculations we explicitly compute both. Phenomenologically, in the regime we will target we find that the moiré modulation slightly decreases the topological gap, in the worst-case scenario by up to a factor three in comparison with the uniform case. In this last moiré superconductor, we now consider the impact of a single strong nonmagnetic impurity per moiré unit cell with $w = 2t$. The electronic structure of the moiré modulated system with a single impurity is shown in Fig. 1(f). It is clearly observed that the gap gets drastically reduced in comparison with the moiré pristine limit of Fig. 1(e). The dramatic impact of the local impurity is a consequence of the unconventional nature of the topological superconducting gap of the moiré heterostructure. While this feature also appears in generic artificial topological superconductors [43–49], the existence of the moiré pattern gives rise to a complex interplay between the local impurity and the moiré length as we address in the next sections.

III. STRONG IMPURITIES IN TOPOLOGICAL MOIRÉ SUPERCONDUCTORS

We now examine in detail the case of a strong-impurity potential. Strong impurities in the effective model are

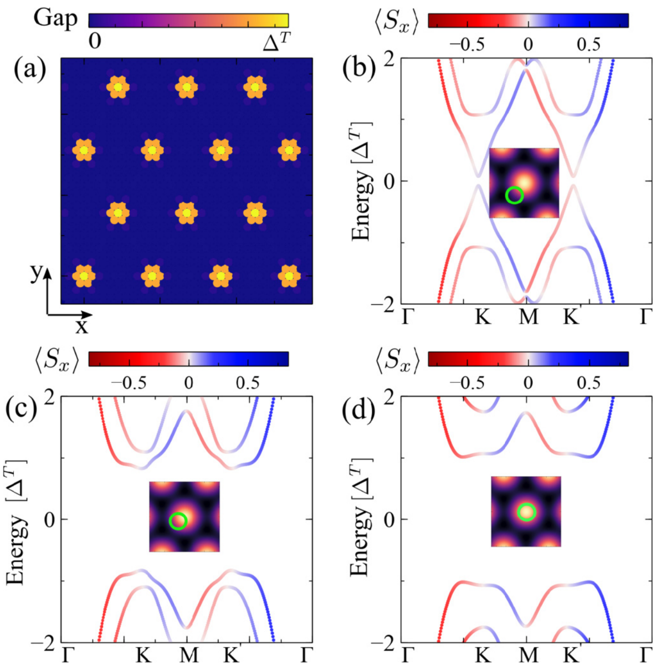

FIG. 2. (a) Gap as a function of impurity location in the strong-impurity regime $w = 2t$. Panels (b), (c), and (d) show the electronic structure for three impurity locations, showing that halfway between exchange maxima, the gap is minimal (b). In comparison, close to the exchange maxima, the gap remains nearly unchanged [(c), (d)]. We used $J_0 = 2\Delta_0$, $\lambda = 2\Delta_0$, $\mu = 3t$, $\delta_J = 2J_0$, $\delta_\Delta = 1.4\Delta_0$.

associated with chemical impurities [41,77–79] and vacancies [80] in the dichalcogenide superconductor, and give rise to a strong scattering center. In particular, for the dichalcogenide superconductor, chemical impurities such as oxygen [42] will give rise to a strong disruption of the electronic structure. Substitutional oxygen impurities, in particular, are expected to create a strong local scattering, comparable to and even higher than the hopping of the low-energy Wannier orbitals [78]. In contrast, atomic replacements such as substitutional S atoms in $NbSe_2$ and $TaSe_2$ would give rise to weaker scattering centers [70,81].

It is worth noting that, since the scattering potential induced by the previous impurities is nonmagnetic, the emergence of in-gap modes stems from the nontrivial nature of the superconducting gap in the moiré system [43]. In particular, nonmagnetic impurities in conventional s-wave superconductors are well known to not give rise to in-gap states as given by Anderson's theorem [82–85]. In contrast, topological superconductors with nonzero Chern number feature in-gap modes in the presence of nonmagnetic impurities, rendering artificial topological superconductors vulnerable to disorder [86–89]. This weakness to disorder stems from the fact that nonmagnetic scattering has a pair-breaking effect [43,83] in unconventional superconductors due to the nontrivial sign structure of the superconducting order [84].

It is first instructive to examine the gap of the moiré system as a function of the location of a strong impurity ($w = 2t$) in a 9×9 supercell, as shown in Fig. 2(a). We focus here on the case with a periodic array of impurities in the system following the moiré pattern, with a single impurity per moiré unit cell, and we keep the same parameter values that we have introduced in Sec. II. Figure 2(a) shows the full gap of the moiré pattern, for a single impurity per moiré unit cell located at each potential location. The gap is measured in units of the topological gap for the topological pristine system Δ^T. In particular, it is observed that the location of the impurity strongly impacts the gap of the system [90]. The resulting gap of the defective system can range from the pristine value, observed for impurities at the exchange maximum, to nearly zero, observed for impurities away from the exchange maximum [Fig. 2(a)]. The previous phenomenology is directly reflected in the electronic band structure for different locations of the impurity [Figs. 2(b)–2(d)]. The electronic structure for an impurity halfway between two exchange maxima is shown in Fig. 2(b), which in particular shows a dramatically smaller gap than the pristine system. In stark contrast, for two locations of the impurities close to the exchange maxima as shown in Figs. 2(c) and 2(d), the gap of the system remains nearly the same as in the pristine system. In particular, the system retains its topologically nontrivial Chern number $C = 2$ with a nearly identical gap for the central impurities shown in Figs. 2(c) and 2(d), whereas the gap is drastically reduced for the location of Fig. 2(b).

The previous phenomenology highlights that the location of the nonmagnetic impurity in the moiré pattern has a critical impact on the superconducting gap of the system. Such strong spatial dependence is fully absent both in nontopological moiré superconductors due to Anderson's theorem [82] and in non-moiré artificial topological superconductors due to the equivalence of the sites.

It is interesting noting that in a moiré superconductor there is a large mismatch between the length scales of the Bloch states and the impurity, in comparison with a uniform superconductor. While there is certainly a mismatch of length scales, our results show that the effect of impurities is comparable both in the absence and presence of a moiré. From the low-energy point of view, a local impurity in real space can be considered like a delta function potential, which creates scattering between all wave vectors in reciprocal space. In the presence of a moiré, the minibands span a small portion of the original Brillouin zone of the material. Nonetheless, due to the mixing between all wave vectors driven by a local impurity, its effect in the minibands is comparable.

IV. WEAK IMPURITIES IN TOPOLOGICAL MOIRÉ SUPERCONDUCTORS

In this section, we examine the electronic structure of the moiré modulated model when a periodic array of weak impurities is distributed in the unit cell, with a single impurity per moiré unit cell. In particular, we examine the evolution of the gap as a function of the impurity location, which highlights the fine interplay between the moiré length and atomic defect. It is worth noting that examining the gap for weak impurities allows tracking small changes in the gap as a function of the impurity location, guaranteeing that the system remains in a topological phase. As noted above, weak impurities would correspond to chalcogen substitution, such as S in $NbSe_2$, leading to a local potential smaller than the bandwidth of the low-energy states.

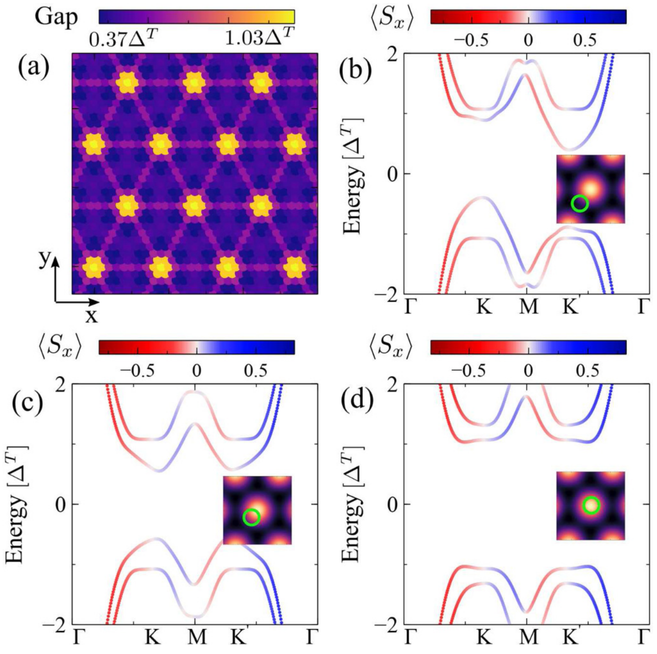

FIG. 3. (a) Gap as a function of impurity location in the weak-impurity regime $w = t/2$. Panels (b), (c), and (d) show the electronic structure for three impurity locations, showing that halfway between exchange maxima, the gap is minimal (b). In contrast, close to the exchange maxima, the gap remains nearly unchanged [(c), (d)]. We used $J_0 = 2\Delta_0$, $\lambda = 2\Delta_0$, $\mu = 3t$, $\delta_J = 2J_0$, $\delta_\Delta = 1.4\Delta_0$.

We first look at the map of the spectral gap as a function of impurity location. We take a moiré unit cell with the size of 9×9, as shown in Fig. 3(a). It is observed that similarly to the strong-impurity regime of Sec. III, the gap remains maximal close to the maximum of the exchange profile, becoming smaller in the other locations of the moiré unit cell. In comparison with the strong-impurity limit, the weak impurity allows keeping a sizable topological gap even for the most detrimental locations away from the exchange maxima. The previous phenomenology can also be observed by examining the electronic structure for different locations of the impurity, shown in Figs. 3(b)–3(d). In particular, it is observed that the electronic structure remains similar for the three impurity locations, apart from small rearrangements that account for the reduced topological gap.

The previous spatial dependence for different impurity locations can be analyzed as a function of the moiré length. The gap for a single impurity per moiré unit cell, computed for different moiré lengths, is shown in Fig. 4, where we consider 11×11 [Fig. 4(a)], 13×13 [Fig. 4(b)], 15×15 [Fig. 4(c)], and 17×17 [Fig. 4(d)]. In particular, we observe that close to the exchange maxima, the local impurity has a relatively weak impact, with the exception of the exact center. Away from the exchange maxima, the impurity shows some of the most sizable effects, having also a complex dependence with the moiré length. This complex dependence naturally emerges from the interplay between the moiré length and the spatial dependence of the in-gap mode, and is intrinsic to any non-magnetic impurity in a moiré topological superconductor. In particular, the interference between the in-gap state and the moiré pattern will be further addressed in Sec. VI, where we will consider a single impurity in an otherwise pristine moiré system.

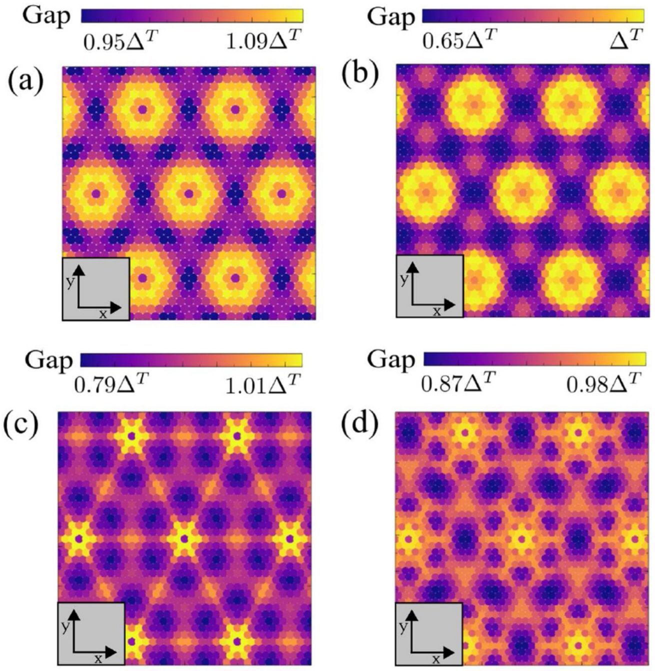

FIG. 4. Topological gap as a function of the location of an impurity in a moiré unit cell, for (a) 11×11, (b) 13×13, (c) 15×15, (d) 17×17 supercells. A direct correlation is observed between the location of the impurity in the unit cell and the moiré pattern, leading to drastic changes in the energy gap. We used $J_0 = 2\Delta_0$, $\lambda = 2\Delta_0$, $\mu = 3t$, $\delta_J = 2J_0$, $\delta_\Delta = 1.4\Delta_0$.

In this section, we have focused on addressing the fine interplay between a periodic array of impurities and the moiré pattern. In particular, one observes a dramatic dependence of the spectral gap on the location of the impurity, directly correlated with the underlying moiré pattern. In contrast with the strong-impurity case, weak impurities will keep the topological gap unchanged, and in particular, all the defective superconducting states of this section show the pristine Chern number $C = 2$.

V. IMPACT OF THE MOIRÉ AMPLITUDE

In a moiré superconductor, the moiré pattern is characterized by the amplitude of the modulation and its average value. In this section, we analyze in detail the effect of moiré amplitude, allowing us to interpolate from the uniform to the modulated limit. In particular, in the uniform limit, the location of the impurity in the unit cell must lead to identical gaps. In contrast, as the moiré pattern is switched on, the gap in the presence of an impurity will develop a strong dependence on its location. To track the evolution with the moiré pattern, we keep the average values of the exchange and superconductivity constant, as well as keeping constant ratios of their modulated amplitude and varying the χ parameter, defined in Eq. (9), between 0 and 1, which allows interpolating between the uniform and moiré limit.

The topological gap for different locations of the impurity and moiré unit cells as a function of the moiré amplitude is

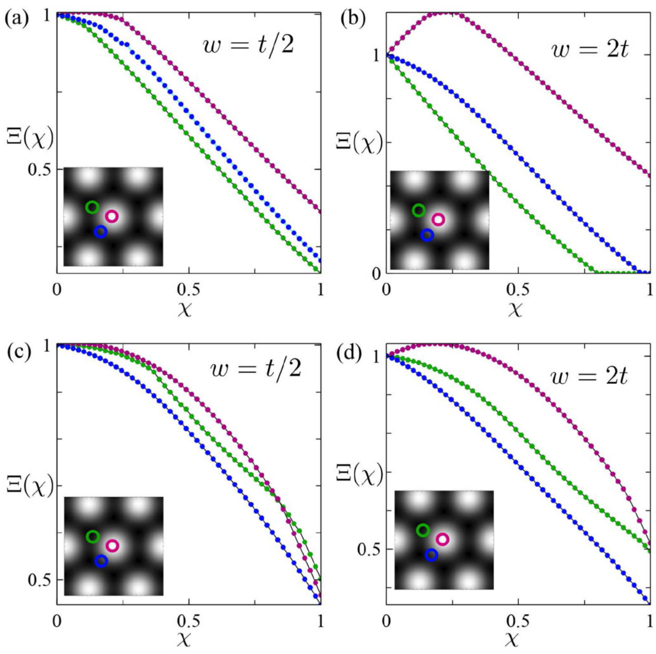

FIG. 5. Normalized topological gap as a function of moiré amplitude [Eq. (15)] for weak [(a), (c)] and strong [(b), (d)] impurity, for a 9×9 [(a), (b)] and a 11×11 [(c), (d)] moiré. It is observed that in the absence of the moiré the location of the impurities does not impact the magnitude of the gap, whereas with moiré, the topological gap shows a strong dependence on the size and location of the impurity. We used $J_0 = 2\Delta_0$, $\lambda = 2\Delta_0$, $\mu = 3t$.

shown in Fig. 5. We consider two different moiré unit cells, a 9×9 moiré unit cell [Figs. 5(a) and 5(b)] and a 11×11 moiré unit cell [Figs. 5(c) and 5(d)], and two strengths of the impurity $w = t/2$ [Figs. 5(a) and 5(c)] and $w = 2t$ [Figs. 5(b) and 5(d)]. For different locations of the impurities, we compute the gap of the moiré system normalized to the gap of a uniform system with impurities,

$$\Xi(\chi) = \frac{\mathcal{G}(\chi, w)}{\mathcal{G}(\chi = 0, w)}, \tag{15}$$

where $\mathcal{G}$ is the gap of the system. The ratio $\Xi(\chi)$ allows us to directly observe the dependence on the location of the impurity for different moiré modulations.

We now focus on the three locations of the impurities shown in Fig. 5, one close to the exchange maximum of the moiré (red), halfway between two exchange maxima (blue), and close to the center formed by three exchange maxima (green). In the absence of a moiré modulation, the three locations lead to the same topological gap, while as the moiré χ is turned on, the gap shows a dependence on the location. In particular, we observe that in most of the instances, the biggest gap is obtained for an impurity close to the exchange maxima (Fig. 5), consistent with the results obtained in Fig. 4. For the locations away from the exchange maxima, the gap is maximized for different locations depending on the moiré length, as observed by comparing Fig. 5(a) with Fig. 5(c), and Fig. 5(b) with Fig. 5(d). This phenomenology is also consistent with the moiré dependence observed in Fig. 4. It is worth noting that, as long as the gap remains open, the Chern number will remain the same all the time. It is finally interesting to note that, for a strong impurity, the location in the moiré unit cell leads to substantially bigger changes in the gap than a weak impurity. This phenomenology is consistent with the results observed in Figs. 2 and 3.

The previous findings highlight that, in the presence of a moiré modulation, the location of an impurity leads to different gaps, especially in the strong-coupling limit. Beyond the cases shown in Fig. 4, we note that even at the center of the unit cell, strong impurities can give rise to a strong impact in the topological phase and ultimately lead to a topological phase transition. For other locations, the topological gap shows a complex interplay between the location of the impurity and the moiré length. These results consider a single impurity per moiré unit cell, leading to strong overlap and interference between each in-gap mode.

We finally comment on what would be the impact if disorder were included in every single site. In such limit, as the strength of the disorder increases, the value of the topological gap will decrease. For weak disorder, the gap will remain finite, yet smaller than the non-disordered case. However, for strong enough uniform disorder, the system will effectively become gapless due to the pair-breaking effect of the impurities. This phenomenology is analogous to other unconventional non-*s*-wave superconductors, where nonmagnetic disorder quenches the underlying topological superconducting gap.

VI. SINGLE-IMPURITY LIMIT

In the sections above, we have focused on considering a periodic array of impurities in the moiré system. Here we will focus on a complementary limit, namely the case of a single impurity on an otherwise pristine moiré system. In this case, the moiré system with a single impurity will lack any type of translational symmetry, and therefore an electronic band structure associated with a moiré Bloch theorem cannot be computed. In order to study the single-impurity limit, we will use the Green's function embedding method, which allows us to compute exactly single defects in otherwise infinite pristine systems [91,92].

The embedding method relies on writing down the Dyson equation for the defective system, that takes the form

$$G_V(\omega) = [\omega - H_V - \Sigma(\omega) + i0^+]^{-1}, \tag{16}$$

where $G_V(\omega)$ is the Green's function of the defective model, H_V the Hamiltonian of the defective unit cell, and $\Sigma(\omega)$ the self-energy induced by the rest of the pristine system. Solving the previous equation requires deriving the self-energy of the pristine system $\Sigma(\omega)$. The self-energy $\Sigma(\omega)$ can be obtained by writing down the Dyson equation for the pristine model

$$G_0(\omega) = [\omega - H_0 - \Sigma(\omega) + i0^+]^{-1}, \tag{17}$$

with H_0 the Hamiltonian of the pristine unit cell. We can now take the Bloch representation of the pristine unit cell Green's function

$$G_0(\omega) = \frac{1}{(2\pi)^2} \int [\omega - H_{\mathbf{k}} + i0^+]^{-1} d^2\mathbf{k}, \tag{18}$$

where $H_{\mathbf{k}}$ is the Bloch Hamiltonian. By obtaining G_0 from Eq. (18), the self-energy $\Sigma(\omega)$ can be obtained from Eq. (17),

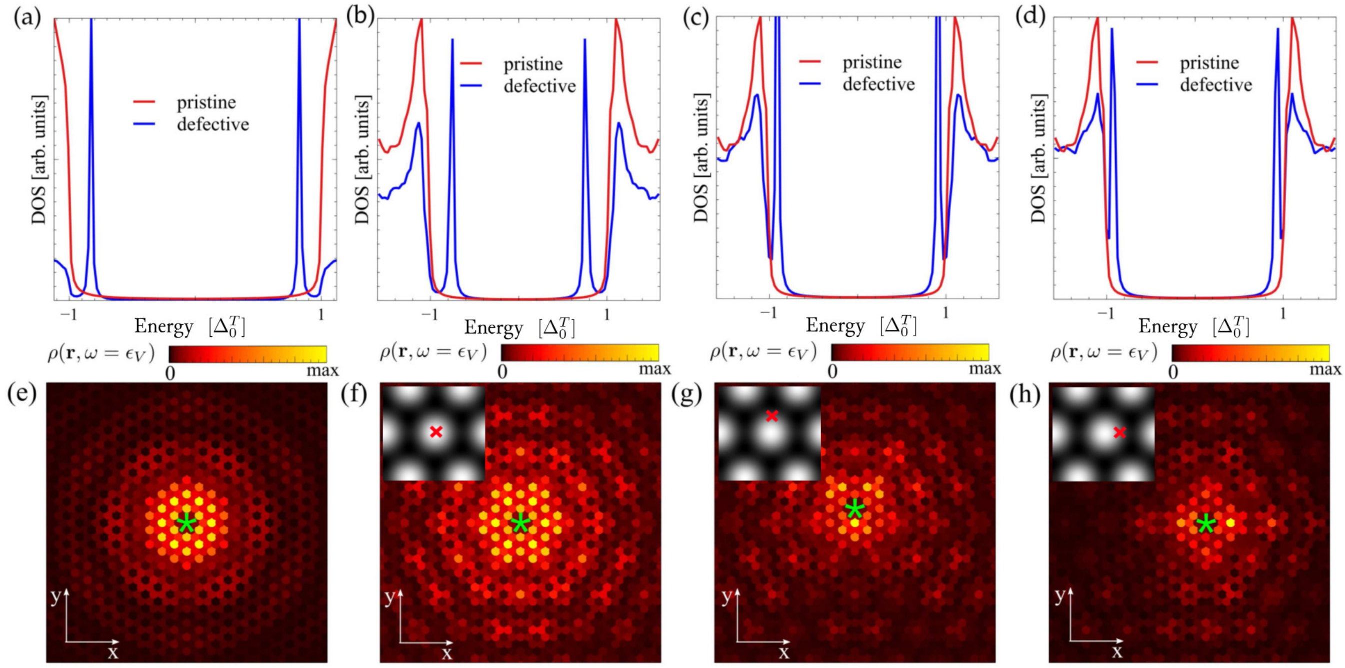

FIG. 6. Density of states [(a)–(d)] and local density of states [(e)–(h)] at the energy of the in-gap state ϵ_V for a single impurity in an otherwise pristine system. Panels (a) and (e) correspond to the uniform case, whereas panels (b), (c), (d), (f), (g), and (h) to different locations of a single impurity [insets in (f), (g), (h)] for the moiré case. Both in the absence (a) and presence [(b), (c), (d)] of a moiré, a strong nonmagnetic impurity gives rise to an in-gap state. It is observed that in the presence of the moiré pattern, the in-gap state leads to a strong interference with moiré length, yielding a spatial dependence with respect to the location of the impurity [(f), (g), (h)]. We used $J_0 = 2\Delta_0$, $\lambda = 2\Delta_0$, $\mu = 3t$, $\delta_J = 2J_0$, $\delta_\Delta = 1.4\Delta_0$, and moiré 5 × 5.

which in turn allows us to obtain the Green's function of the defective unit cell from Eq. (16).

Using the previous methodology, we can extract both the total and local densities of states for a single defect in the moiré topological superconductor. The local density of states $\rho(\mathbf{x},\omega)$ and full density of states $A(\omega)$ are obtained as

$$\rho(\mathbf{x},\omega) = -\frac{1}{\pi}\sum_{s,\tau}\langle \mathbf{x}, s, \tau|\mathrm{Im}[G_V(\omega)]|\mathbf{x}, s, \tau\rangle \tag{19}$$

and

$$\rho(\omega) = -\frac{1}{\pi}\mathrm{Tr}\{\mathrm{Im}[G_V(\omega)]\}, \tag{20}$$

where s runs over spin and τ over electron-hole sector. With the previous methodology, we now compute the density of states with a single impurity for the topological superconductor without the moiré pattern (Fig. 6).

It is first instructive to consider the impurity in the uniform topological superconductor, shown in Figs. 6(a) and 6(e). In particular, it is observed that the existence of a strong nonmagnetic impurity ($w = 2t$) gives rise to an in-gap state [Fig. 6(a)], and that the spatial profile of such in-gap mode is localized around the impurity [Fig. 6(e)] and features intensity oscillations in space. These results in the uniform limit directly suggest that the moiré pattern will give rise to a rich interference pattern with the in-gap state, ultimately responsible for the strong dependence of the location of the impurity observed in previous sections.

We now move on to consider the case with a finite moiré pattern and single impurity, whose density of states is shown in Figs. 6(b)–6(d) and the local density of states is shown in Figs. 6(f)–6(h), for a different location of the impurity with respect to the center of the moiré pattern, shown by the insets in (f)–(h). In particular, we consider three different locations of the impurities. As shown in Figs. 6(b)–6(d) for all the locations of the impurities, we observe in-gap modes at energies ϵ_V. When computing the local density of states associated with those in-gap modes ϵ_V, shown in Figs. 6(f)–6(h), it is observed that the interference pattern between the bound state and the moiré pattern leads to a strong dependence depending on the location of the impurity [93]. Furthermore, it observed that the in-gap mode spans over several moiré unit cells, highlighting that for the periodic array considered in the sections above the in-gap modes between different unit cells have a strong overlap.

The previous results highlight that impurities in the moiré pattern give rise to in-gap states whose wave functions can potentially span over several unit cells, and lead to strong interference effects with the moiré modulation. The previous phenomenology accounts for the strong dependence of the topological gap as a function of the impurity location observed in Sec. IV and Sec. III.

VII. EDGE STATES

Finally, we analyze the emergence of edge states associated with the moiré topological superconducting state in a ribbon with the structure, inset in Figs. 7(d) and 7(h), displaying a schematic of the boundary conditions, which is periodic along the x direction and finite along the y direction.

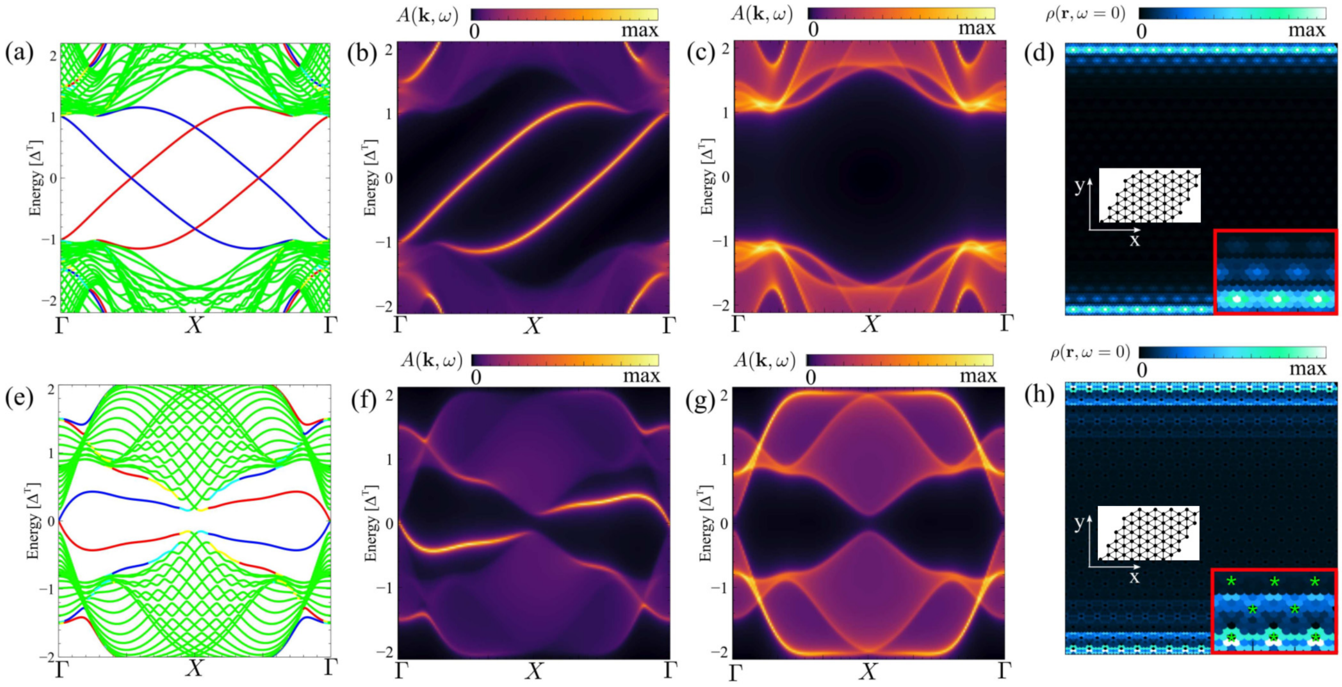

FIG. 7. Moire topological superconducting states of a pristine system [(a), (b), (c), (d)] and of a defective system [(e), (f), (g), (h)]. Panels (a) and (e) show the electronic structure of a ribbon infinite in the x direction and finite in the y direction. Panels (b) and (f) show the momentum-resolved edge spectral function, and panels (c) and (g) the momentum-resolved bulk spectral function. Panels (d) and (h) show the local density of states at $\omega = 0$, highlighting the emergence of topological zero modes at the top and bottom edges following the moiré pattern. The structure insets in (d) and (h) show a schematic of the boundary conditions used. We used $J_0 = 2\Delta_0$, $\lambda = 2\Delta_0$, $\mu = 3t$, $\delta_J = 2J_0$, $\delta_\Delta = 1.4\Delta_0$, and moiré 5 × 5.

In particular, we will consider both pristine and defective cases, and show that in both instances, the edge modes reflect the underlying moiré pattern. We first take a pristine system displaying the moiré topological superconducting state, as shown in Figs. 7(a)–7(d). The electronic structure of a ribbon, infinite in the x direction, is shown in Fig. 7(a), displaying both the existence of a gap in the bulk and propagating edge modes. Those two features are more clearly seen by computing the edge [Fig. 7(b)] and bulk [Fig. 7(c)] spectral functions as shown in Figs. 7(b) and 7(c). $A(\mathbf{k},\omega)$ is the momentum-resolved spectral function in the surface and bulk of a semi-infinite ribbon, with $\mathbf{k}$ the momentum in the translationally invariant direction of the ribbon. It is computed from the momentum-resolved Green's function as $A(\mathbf{k},\omega) = -\frac{1}{\pi}\mathrm{Tr}\{\mathrm{Im}[G(\mathbf{k},\omega)]\}$ where $G(\mathbf{k},\omega)$ is computed with a renormalization algorithm [94]. In particular, it is observed that the edge hosts two co-propagating modes [Fig. 7(b)], consistent with the electronic structure of the moiré ribbon of Fig. 7(a). Beyond the existence of edge modes, the moiré pattern gives rise to a unique feature in real space, namely the modulation of the edge modes following the moiré pattern. This can be clearly seen in Fig. 7(d), where it is observed that the zero-energy modes directly reflect the underlying moiré pattern in the Hamiltonian.

We now move on to consider the defective system. In particular, we focus on a moiré superconductor with a single strong impurity per moiré unit cell. We emphasize that, depending on the location of the impurity and the moiré length, the topological phase can remain the same, become gapless, or a topological phase transition can take place. For the sake of concreteness, here we take a location of an impurity that strongly disrupts the original topological state, giving rise to a topological phase transition to a phase with Chern number $C = -1$. The electronic structure of the defective ribbon is shown in Fig. 7(e), where we observe the existence of a small bulk gap and edge modes. Those modes can be more clearly observed by computing the edge [Fig. 7(f)] and bulk [Fig. 7(g)] spectral function as shown in Figs. 7(f) and 7(g). In particular, the edge spectral function now displays a single edge mode as shown in Fig. 7(f), as expected from the bulk Chern number $C = -1$. It is also observed that the topological edge states avoid the location of the impurity, marked with a green star in Fig. 7(f), as expected from the strong-impurity limit. The edge modes reflect the moiré periodicity again as shown in Fig. 7(h), leading to the imprinting of the moiré pattern in the topological edge modes.

The defective case considered above focuses on a periodic array of strong impurities. In real experiments, impurities can appear either randomly distributed or can be engineered in arrays using atomic manipulation. The first case would correspond to chemical impurities intrinsically appearing during synthesis of the material. In this situation, depending on the density of impurities and their respective location, the original moiré topological phase will be disrupted, either by decreasing its topological gap or ultimately by leading to a gapless state due to the proliferation of in-gap modes. In the situation in which a periodic array of impurities is engineered by means of atomic manipulation [95–105], specific arrangements as those considered in Figs. 7(e)–7(h) can give rise to a topological state with different Chern number. We have verified that solely by changing the location in which the impurity is deposited in the moiré unit cell, the resulting electronic structure could result in topological phases with different Chern number, trivial phases, or even gapless phases. The previous results highlight that atomic manipulation on top of moiré topological superconductors provides a new potential degree of freedom to engineer tunable topological superconductors [106], by exploiting the interplay between the moiré length and local impurities [50–53].

We finally note that this analysis focuses on a minimal model that accounts for the physics of van der Waals ferromagnet/superconductor heterostructures [26–28]. From the quantum chemistry point of view, our model does not account for all the microscopic parameters, but rather focuses on an effective model capturing the physics of this family of heterostructures. In order to provide a microscopically accurate description, calculations would need to be carried out with Wannierization procedures based on first-principles density functional methods [107]. In particular, these methodologies would account for the modulations in all the Hamiltonian parameters, including spin-orbit coupling, hoppings, and on-site energies. Furthermore, relaxation effects would be directly captured with these methodologies [107]. We note, however, that for the current system, first-principles density functional theory methodologies are beyond the computational capabilities, in particular in the presence of spin-orbit coupling, due to the large number of atoms in the unit cell for such a moiré structure. As a results, our discussions focus on a model Hamiltonian, yet without aiming to reach chemical accuracy for $NbSe_2/CrBr_3$ heterostructures.

VIII. CONCLUSION

To summarize, here we addressed the interplay between local impurities and moiré effects in topological moiré superconductors, as those realized in $CrBr_3/NbSe_2$ heterostructures. In particular, our results highlight that, in contrast with conventional artificial topological superconductors, the impact of impurities on a moiré system can give rise to radically different properties depending on their location in the moiré pattern. For strong impurities, we observed that solely depending on the location of the impurity in the moiré pattern, the electronic structure can show a topological gap similar to that in the pristine limit, a nearly gapless state, or a topological phase transition to a topologically different state. For weak impurities, we showed that the topological superconducting gap shows a dependence on both the location of the impurity and the moiré length, yet maintaining its topological nature for all locations. Furthermore, using an embedding formalism we addressed the impact of single nonmagnetic impurities in otherwise infinite pristine moiré systems. In particular, the absence of interference between impurities allows us to clearly identify that the moiré modulation drastically impacts the spatial profile of the in-gap mode created by the nonmagnetic scatterer. Ultimately, we showed that the moiré modulation further emerges in the topological edge modes of the topological superconductor, in both the pristine moiré limit and the defective limit. Our results highlight the rich interplay between local impurities and topological moiré superconductors, and put forward engineered atomic impurities as a powerful and versatile strategy to engineer artificial van der Waals moiré topological superconductors.

ACKNOWLEDGMENTS

We acknowledge the computational resources provided by the Aalto Science-IT project, the financial support from the Academy of Finland Projects No. 331342 and No. 336243, and the Jane and Aatos Erkko Foundation. We thank G. Chen, P. Liljeroth, and S. Kezilebieke for useful discussions.

[1] C. W. J. Beenakker, Search for Majorana fermions in superconductors, Annu. Rev. Condens. Matter Phys. **4**, 113 (2013).

[2] F. Zhang, C. L. Kane, and E. J. Mele, Time-Reversal-Invariant Topological Superconductivity and Majorana Kramers Pairs, Phys. Rev. Lett. **111**, 056402 (2013).

[3] J. Alicea, Y. Oreg, G. Refael, F. von Oppen, and M. P. A. Fisher, Non-Abelian statistics and topological quantum information processing in 1D wire networks, Nat. Phys. **7**, 412 (2011).

[4] B. E. Feldman, M. T. Randeria, J. Li, S. Jeon, Y. Xie, Z. Wang, I. K. Drozdov, B. A. Bernevig, and A. Yazdani, High-resolution studies of the Majorana atomic chain platform, Nat. Phys. **13**, 286 (2017).

[5] S. Nadj-Perge, I. K. Drozdov, J. Li, H. Chen, S. Jeon, J. Seo, A. H. MacDonald, B. A. Bernevig, and A. Yazdani, Observation of Majorana fermions in ferromagnetic atomic chains on a superconductor, Science **346**, 602 (2014).

[6] F. Pientka, L. I. Glazman, and F. von Oppen, Topological superconducting phase in helical Shiba chains, Phys. Rev. B **88**, 155420 (2013).

[7] K. Pöyhönen and T. Ojanen, Superlattice platform for chiral superconductivity with tunable and high Chern numbers, Phys. Rev. B **96**, 174521 (2017).

[8] J. Röntynen and T. Ojanen, Topological Superconductivity and High Chern Numbers in 2D Ferromagnetic Shiba Lattices, Phys. Rev. Lett. **114**, 236803 (2015).

[9] A. R. Akhmerov, J. Nilsson, and C. W. J. Beenakker, Electrically Detected Interferometry of Majorana Fermions in a Topological Insulator, Phys. Rev. Lett. **102**, 216404 (2009).

[10] D. Sticlet, C. Bena, and P. Simon, Spin and Majorana Polarization in Topological Superconducting Wires, Phys. Rev. Lett. **108**, 096802 (2012).

[11] J. Klinovaja, P. Stano, A. Yazdani, and D. Loss, Topological Superconductivity and Majorana Fermions in RKKY Systems, Phys. Rev. Lett. **111**, 186805 (2013).

[12] J. L. Lado and M. Sigrist, Two-Dimensional Topological Superconductivity with Antiferromagnetic Insulators, Phys. Rev. Lett. **121**, 037002 (2018).

[13] A. Kreisel, T. Hyart, and B. Rosenow, Tunable topological states hosted by unconventional superconductors with adatoms, Phys. Rev. Res. **3**, 033049 (2021).

[14] P. San-Jose, J. L. Lado, R. Aguado, F. Guinea, and J. Fernández-Rossier, Majorana Zero Modes in Graphene, Phys. Rev. X **5**, 041042 (2015).

[15] X.-L. Qi and S.-C. Zhang, Topological insulators and superconductors, Rev. Mod. Phys. **83**, 1057 (2011).

[16] J. Alicea, New directions in the pursuit of Majorana fermions in solid state systems, Rep. Prog. Phys. **75**, 076501 (2012).

[17] D. Aasen, M. Hell, R. V. Mishmash, A. Higginbotham, J. Danon, M. Leijnse, T. S. Jespersen, J. A. Folk, C. M. Marcus, K. Flensberg, and J. Alicea, Milestones toward Majorana-Based Quantum Computing, Phys. Rev. X **6**, 031016 (2016).

[18] J. D. Sau, R. M. Lutchyn, S. Tewari, and S. Das Sarma, Generic New Platform for Topological Quantum Computation Using Semiconductor Heterostructures, Phys. Rev. Lett. **104**, 040502 (2010).

[19] Y. Oreg, G. Refael, and F. von Oppen, Helical Liquids and Majorana Bound States in Quantum Wires, Phys. Rev. Lett. **105**, 177002 (2010).

[20] V. Mourik, K. Zuo, S. M. Frolov, S. R. Plissard, E. P. A. M. Bakkers, and L. P. Kouwenhoven, Signatures of Majorana fermions in hybrid superconductor-semiconductor nanowire devices, Science **336**, 1003 (2012).

[21] M. T. Deng, S. Vaitiekėnas, E. B. Hansen, J. Danon, M. Leijnse, K. Flensberg, J. Nygård, P. Krogstrup, and C. M. Marcus, Majorana bound state in a coupled quantum-dot hybrid-nanowire system, Science **354**, 1557 (2016).

[22] A. Das, Y. Ronen, Y. Most, Y. Oreg, M. Heiblum, and H. Shtrikman, Zero-bias peaks and splitting in an Al-InAs nanowire topological superconductor as a signature of Majorana fermions, Nat. Phys. **8**, 887 (2012).

[23] L. Schneider, P. Beck, T. Posske, D. Crawford, E. Mascot, S. Rachel, R. Wiesendanger, and J. Wiebe, Topological Shiba bands in artificial spin chains on superconductors, Nat. Phys. **17**, 943 (2021).

[24] F. Lüpke, D. Waters, S. C. de la Barrera, M. Widom, D. G. Mandrus, J. Yan, R. M. Feenstra, and B. M. Hunt, Proximity-induced superconducting gap in the quantum spin Hall edge state of monolayer WTe_2, Nat. Phys. **16**, 526 (2020).

[25] B. Jäck, Y. Xie, J. Li, S. Jeon, B. A. Bernevig, and A. Yazdani, Observation of a Majorana zero mode in a topologically protected edge channel, Science **364**, 1255 (2019).

[26] S. Kezilebieke, Md N. Huda, V. Vaňo, M. Aapro, S. C. Ganguli, O. J. Silveira, S. Głodzik, A. S. Foster, T. Ojanen, and P. Liljeroth, Topological superconductivity in a van der waals heterostructure, Nature (London) **588**, 424 (2020).

[27] S. Kezilebieke, O. J. Silveira, Md N. Huda, V. Vaňo, M. Aapro, S. C. Ganguli, J. Lahtinen, R. Mansell, S. Dijken, A. S. Foster, and P. Liljeroth, Electronic and magnetic characterization of epitaxial $CrBr_3$ monolayers on a superconducting substrate, Adv. Mater. **33**, 2006850 (2021).

[28] S. Kezilebieke, V. Vaňo, Md N. Huda, M. Aapro, S. C. Ganguli, P. Liljeroth, and J. L. Lado, Moiré-enabled topological superconductivity, Nano Lett. **22**, 328 (2022).

[29] A. K. Geim and I. V. Grigorieva, Van der Waals heterostructures, Nature (London) **499**, 419 (2013).

[30] Y. Liu, N. O. Weiss, X. Duan, H.-C. Cheng, Y. Huang, and X. Duan, Van der Waals heterostructures and devices, Nat. Rev. Mater. **1**, 16042 (2016).

[31] J. M. B. Lopes dos Santos, N. M. R. Peres, and A. H. Castro Neto, Graphene Bilayer with a Twist: Electronic Structure, Phys. Rev. Lett. **99**, 256802 (2007).

[32] E. Suárez Morell, J. D. Correa, P. Vargas, M. Pacheco, and Z. Barticevic, Flat bands in slightly twisted bilayer graphene: Tight-binding calculations, Phys. Rev. B **82**, 121407(R) (2010).

[33] R. Bistritzer and A. H. MacDonald, Moiré bands in twisted double-layer graphene, Proc. Natl. Acad. Sci. USA **108**, 12233 (2011).

[34] S. Fang and E. Kaxiras, Electronic structure theory of weakly interacting bilayers, Phys. Rev. B **93**, 235153 (2016).

[35] A. O. Sboychakov, A. L. Rakhmanov, A. V. Rozhkov, and F. Nori, Electronic spectrum of twisted bilayer graphene, Phys. Rev. B **92**, 075402 (2015).

[36] T. Song, Q.-C. Sun, E. Anderson, C. Wang, J. Qian, T. Taniguchi, K. Watanabe, M. A. McGuire, R. Stöhr, D. Xiao, T. Cao, J. Wrachtrup, and X. Xu, Direct visualization of magnetic domains and moiré magnetism in twisted 2D magnets, Science **374**, 1140 (2021).

[37] T. I. Andersen, G. Scuri, A. Sushko, K. De Greve, J. Sung, Y. Zhou, D. S. Wild, R. J. Gelly, H. Heo, D. Bérubé, A. Y. Joe, L. A. Jauregui, K. Watanabe, T. Taniguchi, P. Kim, H. Park, and M. D. Lukin, Excitons in a reconstructed moiré potential in twisted WSe_2/WSe_2 homobilayers, Nat. Mater. **20**, 480 (2021).

[38] E. V. Castro, M. P. López-Sancho, and M. A. H. Vozmediano, New Type of Vacancy-Induced Localized States in Multilayer Graphene, Phys. Rev. Lett. **104**, 036802 (2010).

[39] M. M. Ugeda, I. Brihuega, F. Guinea, and J. M. Gómez-Rodríguez, Missing Atom as a Source of Carbon Magnetism, Phys. Rev. Lett. **104**, 096804 (2010).

[40] L. Nguyen, H.-P. Komsa, E. Khestanova, R. J. Kashtiban, J. J. P. Peters, S. Lawlor, A. M. Sanchez, J. Sloan, R. V. Gorbachev, I. V. Grigorieva, A. V. Krasheninnikov, and S. J. Haigh, Atomic defects and doping of monolayer $NbSe_2$, ACS Nano **11**, 2894 (2017).

[41] S. Wang, A. Robertson, and J. H. Warner, Atomic structure of defects and dopants in 2D layered transition metal dichalcogenides, Chem. Soc. Rev. **47**, 6764 (2018).

[42] S. Barja, S. Refaely-Abramson, B. Schuler, D. Y. Qiu, A. Pulkin, S. Wickenburg, H. Ryu, M. M. Ugeda, C. Kastl, C. Chen, C. Hwang, A. Schwartzberg, S. Aloni, S.-K. Mo, D. F. Ogletree, M. F. Crommie, O. V. Yazyev, S. G. Louie, J. B. Neaton, and A. Weber-Bargioni, Identifying substitutional oxygen as a prolific point defect in monolayer transition metal dichalcogenides, Nat. Commun. **10**, 3382 (2019).

[43] A. V. Balatsky, I. Vekhter, and J.-X. Zhu, Impurity-induced states in conventional and unconventional superconductors, Rev. Mod. Phys. **78**, 373 (2006).

[44] A. M. Black-Schaffer, A. V. Balatsky, and J. Fransson, Filling of magnetic-impurity-induced gap in topological insulators by potential scattering, Phys. Rev. B **91**, 201411(R) (2015).

[45] I. C. Fulga, B. van Heck, M. Burrello, and T. Hyart, Effects of disorder on Coulomb-assisted braiding of Majorana zero modes, Phys. Rev. B **88**, 155435 (2013).

[46] L. Kimme and T. Hyart, Existence of zero-energy impurity states in different classes of topological insulators and superconductors and their relation to topological phase transitions, Phys. Rev. B **93**, 035134 (2016).

[47] K. Pöyhönen, A. Westström, and T. Ojanen, Topological superconductivity in ferromagnetic atom chains beyond the deep-impurity regime, Phys. Rev. B **93**, 014517 (2016).

[48] V. Kaladzhyan, C. Bena, and P. Simon, Asymptotic behavior of impurity-induced bound states in low-dimensional topological superconductors, J. Phys.: Condens. Matter **28**, 485701 (2016).

[49] Y.-Y. Tai, H. Choi, T. Ahmed, C. S. Ting, and J.-X. Zhu, Edge states and local electronic structure around an adsorbed impurity in a topological superconductor, Phys. Rev. B **92**, 174514 (2015).

[50] I. Brihuega and F. Yndurain, Selective hydrogen adsorption in graphene rotated bilayers, J. Phys. Chem. B **122**, 595 (2018).

[51] A. Ramires and J. L. Lado, Impurity-induced triple point fermions in twisted bilayer graphene, Phys. Rev. B **99**, 245118 (2019).

[52] A. Lopez-Bezanilla and J. L. Lado, Electrical band flattening, valley flux, and superconductivity in twisted trilayer graphene, Phys. Rev. Res. **2**, 033357 (2020).

[53] A. Lopez-Bezanilla and J. L. Lado, Defect-induced magnetism and Yu-Shiba-Rusinov states in twisted bilayer graphene, Phys. Rev. Mater. **3**, 084003 (2019).

[54] T. Naimer, K. Zollner, M. Gmitra, and J. Fabian, Twist-angle dependent proximity induced spin-orbit coupling in graphene/transition metal dichalcogenide heterostructures, Phys. Rev. B **104**, 195156 (2021).

[55] K. Zollner and J. Fabian, Bilayer graphene encapsulated within monolayers of WS_2 or $Cr_2Ge_2Te_6$: Tunable proximity spin-orbit or exchange coupling, Phys. Rev. B **104**, 075126 (2021).

[56] P. Högl, T. Frank, K. Zollner, D. Kochan, M. Gmitra, and J. Fabian, Quantum Anomalous Hall Effects in Graphene from Proximity-Induced Uniform and Staggered Spin-Orbit and Exchange Coupling, Phys. Rev. Lett. **124**, 136403 (2020).

[57] X. Hu, N. Mao, H. Wang, Y. Dai, B. Huang, and C. Niu, Quantum spin Hall effect in antiferromagnetic topological heterobilayers, Phys. Rev. B **103**, 085109 (2021).

[58] B. Karpiak, A. W. Cummings, K. Zollner, M. Vila, D. Khokhriakov, A. Md Hoque, A. Dankert, P. Svedlindh, J. Fabian, S. Roche, and S. P. Dash, Magnetic proximity in a van der Waals heterostructure of magnetic insulator and graphene, 2D Mater. **7**, 015026 (2020).

[59] G. Cantele, D. Alfè, F. Conte, V. Cataudella, D. Ninno, and P. Lucignano, Structural relaxation and low-energy properties of twisted bilayer graphene, Phys. Rev. Res. **2**, 043127 (2020).

[60] L. Zhang, Z. Zhang, F. Wu, D. Wang, R. Gogna, S. Hou, K. Watanabe, T. Taniguchi, K. Kulkarni, T. Kuo, S. R. Forrest, and H. Deng, Twist-angle dependence of moiré excitons in $WS_2/MoSe_2$ heterobilayers, Nat. Commun. **11**, 5888 (2020).

[61] N. Ubrig, Z. Wang, J. Teyssier, T. Taniguchi, K. Watanabe, E. Giannini, A. F. Morpurgo, and M. Gibertini, Low-temperature monoclinic layer stacking in atomically thin CrI_3 crystals, 2D Mater. **7**, 015007 (2020).

[62] D. J. Trainer, B. K. Wang, F. Bobba, N. Samuelson, X. Xi, J. Zasadzinski, J. Nieminen, A. Bansil, and M. Iavarone, Proximity-induced superconductivity in monolayer MoS_2, ACS Nano **14**, 2718 (2020).

[63] M. Kim, P. Kumaravadivel, J. Birkbeck, W. Kuang, S. G. Xu, D. G. Hopkinson, J. Knolle, P. A. McClarty, A. I. Berdyugin, M. B. Shalom, R. V. Gorbachev, S. J. Haigh, S. Liu, J. H. Edgar, K. S. Novoselov, I. V. Grigorieva, and A. K. Geim, Micromagnetometry of two-dimensional ferromagnets, Nat. Electron. **2**, 457 (2019).

[64] B. Huang, G. Clark, E. Navarro-Moratalla, D. R. Klein, R. Cheng, K. L. Seyler, D. Zhong, E. Schmidgall, M. A. McGuire, D. H. Cobden, W. Yao, D. Xiao, P. Jarillo-Herrero, and X. Xu, Layer-dependent ferromagnetism in a van der Waals crystal down to the monolayer limit, Nature (London) **546**, 270 (2017).

[65] T. A. Tartaglia, J. N. Tang, J. L. Lado, F. Bahrami, M. Abramchuk, G. T. McCandless, M. C. Doyle, K. S. Burch, Y. Ran, J. Y. Chan, and F. Tafti, Accessing new magnetic regimes by tuning the ligand spin-orbit coupling in van der Waals magnets, Sci. Adv. **6**, eabb9379 (2020).

[66] M. M. Ugeda, A. J. Bradley, Y. Zhang, S. Onishi, Y. Chen, W. Ruan, C. Ojeda-Aristizabal, H. Ryu, M. T. Edmonds, H.-Z. Tsai, A. Riss, S.-K. Mo, D. Lee, A. Zettl, Z. Hussain, Z.-X. Shen, and M. F. Crommie, Characterization of collective ground states in single-layer $NbSe_2$, Nat. Phys. **12**, 92 (2016).

[67] R. Yan, G. Khalsa, B. T. Schaefer, A. Jarjour, S. Rouvimov, K. C. Nowack, H. G. Xing, and D. Jena, Thickness dependence of superconductivity in ultrathin NbS_2, Appl. Phys. Express **12**, 023008 (2019).

[68] E. Navarro-Moratalla, J. O. Island, S. Mañas-Valero, E. Pinilla-Cienfuegos, A. Castellanos-Gomez, J. Quereda, G. Rubio-Bollinger, L. Chirolli, J. A. Silva-Guillén, N. Agraït, G. A. Steele, F. Guinea, H. S. J. van der Zant, and E. Coronado, Enhanced superconductivity in atomically thin TaS_2, Nat. Commun. **7**, 11043 (2016).

[69] C.-S. Lian, C. Heil, X. Liu, C. Si, F. Giustino, and W. Duan, Coexistence of superconductivity with enhanced charge density wave order in the two-dimensional limit of $TaSe_2$, J. Phys. Chem. Lett. **10**, 4076 (2019).

[70] K. Zhao, H. Lin, X. Xiao, W. Huang, W. Yao, M. Yan, Y. Xing, Q. Zhang, Z.-X. Li, S. Hoshino, J. Wang, S. Zhou, L. Gu, M. S. Bahramy, H. Yao, N. Nagaosa, Q.-K. Xue, K. T. Law, X. Chen, and S.-H. Ji, Disorder-induced multifractal superconductivity in monolayer niobium dichalcogenides, Nat. Phys. **15**, 904 (2019).

[71] M. Khosravian and J. L. Lado, Quasiperiodic criticality and spin-triplet superconductivity in superconductor-antiferromagnet moiré patterns, Phys. Rev. Res. **3**, 013262 (2021).

[72] D. Soriano, C. Cardoso, and J. Fernández-Rossier, Interplay between interlayer exchange and stacking in CrI_3 bilayers, Solid State Commun. **299**, 113662 (2019).

[73] N. Sivadas, S. Okamoto, X. Xu, C. J. Fennie, and D. Xiao, Stacking-dependent magnetism in bilayer CrI_3, Nano Lett. **18**, 7658 (2018).

[74] P. G. de Gennes and P. A. Pincus, *Superconductivity of Metals and Alloys*, 1st ed. (CRC Press, Boca Raton, 1999).

[75] A. I. Buzdin, Proximity effects in superconductor-ferromagnet heterostructures, Rev. Mod. Phys. **77**, 935 (2005).

[76] Y. Noat, J. A. Silva-Guillén, T. Cren, V. Cherkez, C. Brun, S. Pons, F. Debontridder, D. Roditchev, W. Sacks, L. Cario, P. Ordejón, A. García, and E. Canadell, Quasiparticle spectra of $2H$-$NbSe_2$: Two-band superconductivity and the role of tunneling selectivity, Phys. Rev. B **92**, 134510 (2015).

[77] Z. Lin, B. R. Carvalho, E. Kahn, R. Lv, R. Rao, H. Terrones, M. A. Pimenta, and M. Terrones, Defect engineering of two-dimensional transition metal dichalcogenides, 2D Mater. **3**, 022002 (2016).

[78] S. Haldar, H. Vovusha, M. K. Yadav, O. Eriksson, and B. Sanyal, Systematic study of structural, electronic, and optical properties of atomic-scale defects in the two-dimensional transition metal dichalcogenides MX_2 (M = Mo, W; X = S, Se, Te), Phys. Rev. B **92**, 235408 (2015).

[79] M. Mahjouri-Samani, L. Liang, A. Oyedele, Y.-S. Kim, M. Tian, N. Cross, K. Wang, M.-W. Lin, A. Boulesbaa, C. M. Rouleau, A. A. Puretzky, K. Xiao, M. Yoon, G. Eres, G. Duscher, B. G. Sumpter, and D. B. Geohegan, Tailoring vacancies far beyond intrinsic levels changes the carrier type and optical response in monolayer $MoSe_{2-x}$ crystals, Nano Lett. **16**, 5213 (2016).

[80] M. Pandey, F. A. Rasmussen, K. Kuhar, T. Olsen, K. W. Jacobsen, and K. S. Thygesen, Defect-tolerant monolayer transition metal dichalcogenides, Nano Lett. **16**, 2234 (2016).

[81] L. Li, X. Deng, Z. Wang, Y. Liu, M. Abeykoon, E. Dooryhee, A. Tomic, Y. Huang, J. B. Warren, E. S. Bozin, S. J. L. Billinge, Y. Sun, Y. Zhu, G. Kotliar, and C. Petrovic, Superconducting order from disorder in $2H$-$TaSe_{2-x}S_x$, npj Quantum Mater. **2**, 11 (2017).

[82] P. W. Anderson, Theory of dirty superconductors, J. Phys. Chem. Solids **11**, 26 (1959).

[83] A. Ramires and M. Sigrist, Identifying detrimental effects for multiorbital superconductivity: Application to Sr_2RuO_4, Phys. Rev. B **94**, 104501 (2016).

[84] A. Ramires, D. F. Agterberg, and M. Sigrist, Tailoring T_c by symmetry principles: The concept of superconducting fitness, Phys. Rev. B **98**, 024501 (2018).

[85] A. Ramires, Nonunitary superconductivity in complex quantum materials, J. Phys.: Condens. Matter **34**, 304001 (2022).

[86] N. M. Gergs, L. Fritz, and D. Schuricht, Topological order in the Kitaev/Majorana chain in the presence of disorder and interactions, Phys. Rev. B **93**, 075129 (2016).

[87] S. S. Hegde and S. Vishveshwara, Majorana wave-function oscillations, fermion parity switches, and disorder in Kitaev chains, Phys. Rev. B **94**, 115166 (2016).

[88] E. Prada, P. San-Jose, M. W. A. de Moor, A. Geresdi, E. J. H. Lee, J. Klinovaja, D. Loss, J. Nygård, R. Aguado, and L. P. Kouwenhoven, From Andreev to Majorana bound states in hybrid superconductor-semiconductor nanowires, Nat. Rev. Phys. **2**, 575 (2020).

[89] L. Andersen, A. Ramires, Z. Wang, T. Lorenz, and Y. Ando, Generalized Anderson's theorem for superconductors derived from topological insulators, Sci. Adv. **6**, eaay6502 (2020).

[90] B. Zinkl and A. Ramires, Sensitivity of superconducting states to the impurity location in layered materials, Phys. Rev. B **106**, 014515 (2022).

[91] J. L. Lado and J. Fernández-Rossier, Unconventional Yu-Shiba-Rusinov states in hydrogenated graphene, 2D Mater. **3**, 025001 (2016).

[92] G. Chen and J. L. Lado, Impurity-induced resonant spinon zero modes in Dirac quantum spin liquids, Phys. Rev. Res. **2**, 033466 (2020).

[93] E. Liebhaber, S. A. González, R. Baba, G. Reecht, B. W. Heinrich, S. Rohlf, K. Rossnagel, F. von Oppen, and K. J. Franke, Yu-Shiba-Rusinov states in the charge-density modulated superconductor $NbSe_2$, Nano Lett. **20**, 339 (2020).

[94] M. P. L. Sancho, J. M. L. Sancho, J. M. L. Sancho, and J. Rubio, Highly convergent schemes for the calculation of bulk and surface Green functions, J. Phys. F **15**, 851 (1985).

[95] C. F. Hirjibehedin, C. P. Lutz, and A. J. Heinrich, Spin coupling in engineered atomic structures, Science **312**, 1021 (2006).

[96] F. E. Kalff, M. P. Rebergen, E. Fahrenfort, J. Girovsky, R. Toskovic, J. L. Lado, J. Fernández-Rossier, and A. F. Otte, A kilobyte rewritable atomic memory, Nat. Nanotechnol. **11**, 926 (2016).

[97] D.-J. Choi, N. Lorente, J. Wiebe, K. von Bergmann, A. F. Otte, and A. J. Heinrich, Colloquium: Atomic spin chains on surfaces, Rev. Mod. Phys. **91**, 041001 (2019).

[98] R. Drost, T. Ojanen, A. Harju, and P. Liljeroth, Topological states in engineered atomic lattices, Nat. Phys. **13**, 668 (2017).

[99] M. R. Slot, T. S. Gardenier, P. H. Jacobse, G. C. P. van Miert, S. N. Kempkes, S. J. M. Zevenhuizen, C. M. Smith, D. Vanmaekelbergh, and I. Swart, Experimental realization and characterization of an electronic Lieb lattice, Nat. Phys. **13**, 672 (2017).

[100] K. Yang, S.-H. Phark, Y. Bae, T. Esat, P. Willke, A. Ardavan, A. J. Heinrich, and C. P. Lutz, Probing resonating valence bond states in artificial quantum magnets, Nat. Commun. **12**, 993 (2021).

[101] F. von Oppen and K. J. Franke, Yu-Shiba-Rusinov states in real metals, Phys. Rev. B **103**, 205424 (2021).

[102] H. González-Herrero, J. M. Gómez-Rodríguez, P. Mallet, M. Moaied, J. J. Palacios, C. Salgado, M. M. Ugeda, J.-Y. Veuillen, F. Yndurain, and I. Brihuega, Atomic-scale control of graphene magnetism by using hydrogen atoms, Science **352**, 437 (2016).

[103] Md N. Huda, S. Kezilebieke, and P. Liljeroth, Designer flat bands in quasi-one-dimensional atomic lattices, Phys. Rev. Res. **2**, 043426 (2020).

[104] S. Kezilebieke, M. Dvorak, T. Ojanen, and P. Liljeroth, Coupled Yu-Shiba-Rusinov states in molecular dimers on $NbSe_2$, Nano Lett. **18**, 2311 (2018).

[105] S. Kezilebieke, R. Žitko, M. Dvorak, T. Ojanen, and P. Liljeroth, Observation of coexistence of Yu-Shiba-Rusinov states and spin-flip excitations, Nano Lett. **19**, 4614 (2019).

[106] D. Sticlet and C. Morari, Topological superconductivity from magnetic impurities on monolayer $NbSe_2$, Phys. Rev. B **100**, 075420 (2019).

[107] M. H. Naik and M. Jain, Ultraflatbands and Shear Solitons in Moiré Patterns of Twisted Bilayer Transition Metal Dichalcogenides, Phys. Rev. Lett. **121**, 266401 (2018).